Available online at www.sciencedirect.com
ScienceDirect
Journal of Power Sources 167 (2007) 118–129
JOURNAL OF POWER SOURCES
www.elsevier.com/locate/jpowsour

Engineering model of a passive planar air breathing fuel cell cathode

Ryan O'Hayre [a,*], Tibor Fabian [b], Shawn Litster [b], Fritz B. Prinz [b], Juan G. Santiago [b]

[a] *Department of Metallurgical and Materials Engineering, Colorado School of Mines, Golden, CO 80401, United States*
[b] *Department of Mechanical Engineering, Stanford University, Stanford, CA 94305, United States*

Received 8 December 2006; received in revised form 30 January 2007; accepted 30 January 2007
Available online 6 February 2007

Abstract

The behavior of an air breathing fuel cell (ABFC) operated on dry-hydrogen in dead-ended mode is studied using theoretical analysis. A one-dimensional, non-isothermal, combined heat and mass transport model is developed that captures the coupling between water generation, oxygen consumption, self-heating and natural convection at the air breathing cathode. The model is validated against planar ABFC experimental measurements over a range of ambient temperatures. The model confirms the strong effect of self-heating on the water balance within passive ABFCs. Model analysis provides several conclusions: (1) thermal runaway caused by inadequate heat rejection predominantly limits ABFC performance. (2) The natural convection boundary layer represents a significant barrier to cathode mass and heat transfer. (3) Because the mass and heat transport numbers associated with natural convection are small, even slight forced convection dramatically affects cell behavior. (4) Performance optimization requires maximizing heat rejection while minimizing flooding. Decoupling the latter two phenomena is challenging due to the exponential relationship between water vapor saturation and temperature.

Keywords: Natural convection; Mixed heat and mass transfer; Modeling planar fuel cell; Dead-ended anode

1. Introduction

Air breathing polymer electrolyte membrane fuel cells (PEMFCs) use free convection airflow to supply oxygen to their cathodes. These cells are typically characterized by low output power densities compared to forced-convection fuel cells. They are nevertheless attractive for portable-power applications [1,2] where the simplicity of free-convection oxidant delivery can outweigh the cost, complexity, noise and the parasitic power consumption introduced by active system design. However, the inability to regulate the air stream conditions (flow stochiometry, temperature, humidity) makes water-balanced operation of an air breathing fuel cell particularly challenging.

Planar air breathing cells are characterized by an open cathode structure that allows ambient air to advect and diffuse to the surface, while simultaneously collecting current from a gas diffusion layer [3,4]. Planar air breathing fuel cells offer the advantage of a flat form factor suitable for small portable applications. There have been several recent experimental [3–10] and modeling [11–16] studies on planar air breathing fuel cells. In one of the few combined experimental and modeling studies of an air breathing PEMFC, Mennola et al. concluded that their fuel cell was limited by water removal at 40 °C and by oxygen depletion at 60 °C [14]. In related work, the same group highlighted the importance of developing a significant temperature gradient between the fuel cell and the air to drive efficient oxygen transport to the cathode [17]. Li et al. theoretically analyzed convective mass transfer at a free-breathing fuel cell cathode but did not consider thermal gradients [13]. Their analysis concluded that free-breathing fuel cell performance is significantly limited at high current densities due to oxygen mass transfer considerations. Ying et al. developed a 3D model for an air breathing PEMFC that considered both heat and mass transfer [11,12]. Their model was applied to channel-type air breathing fuel cells, rather than planar open-cathode fuel cells. In such cells, performance was shown to depend strongly on the cathode channel geometry. Litster et al. [16] computationally resolved the natural convection and mass transfer above the open cathode of an air breathing non-planar PEMFC. Their results indicated significant self-heating in fuel cells cooled only by natural convection.

In this paper, we develop a simple one-dimensional engineering model for a planar air breathing fuel cell that considers the

* Corresponding author at: Department of Metallurgical and Materials Engineering, Colorado School of Mines, Golden, CO 80401, United States.
Tel.: +1 303 273 3952; fax: +1 303 273 3795.

0378-7753/$ – see front matter © 2007 Elsevier B.V. All rights reserved.
doi:10.1016/j.jpowsour.2007.01.073

mixed heat and mass transfer situation at the open cathode. Our model is based on a theoretical analysis of free convection heat and mass transfer, and these dynamics are coupled to the rate of heat production and species generation/depletion at the fuel cell cathode. This simplified engineering analysis provides an intuitive understanding of the primary factors driving the performance of planar air breathing fuel cells. Furthermore, the model qualitatively reproduces the experimentally observed behavior of a planar air breathing fuel cell over a range of operating conditions (T_{ambient} 10–30 °C). Lastly, the model is used to explore the limits of air breathing fuel cell operation.

2. Free convection heat and mass transfer analysis

The natural convection above the surface of an open fuel cell cathode is characterized by the simultaneous transport of thermal energy, momentum, and chemical species. Heat production within the fuel cell creates temperature gradients above the cathode surface, while oxygen consumption and water production give rise to concentration gradients of molecular oxygen and water vapor. The air density above the cathode surface, and consequently the rate of natural convection, is affected by all three gradients. In this section, we apply free convection heat and mass transfer analysis to determine the heat, oxygen and water transfer coefficients (h_{T}, h_{O_2} and $h_{\text{H}_2\text{O}}$, respectively) that describe transport within the boundary layer between the cathode surface and free air.

Natural convection driven exclusively by thermal gradients is described by the non-dimensional heat transfer coefficient, Nu_L, the Nusselt number, based on a characteristic system length L. Empirical formulae exist (see e.g. ref. [18]) for many practical geometries and boundary conditions that correlate Nu_L with other non-dimensional groups such as the Grashof number (Gr_L) and the Prandtl number (Pr). In general, $\overline{Nu_L} = f(Gr_L, Pr)$. In an analogous fashion, natural convection driven exclusively by concentration gradients may be described by the non-dimensional mass transfer coefficient, Sh_L, the Sherwood number. The Sherwood number, in turn, can also be related to other non-dimensional groups as $\overline{Sh_L} = f(Gr_L, Sc)$, where Sc is the Schmidt number.

Similarity considerations for natural convection driven by *concurrent* temperature and concentration gradients yield $\overline{Nu_L} = f(Gr_L, Pr, Sc)$ and $\overline{Sh_L} = f(Gr_L, Sc, Pr)$. However, as a first approximation the simpler correlations given for Nu_L and Sh_L may be used to determine the heat and mass transfer coefficients provided the effects of temperature and concentration on density are properly accounted for [18]. The Prandtl number is defined as $Pr = \nu/\alpha$, where ν is the kinematic viscosity and α is the thermal diffusivity. In a similar manner, the Schmidt number is defined as $Sc = \nu/D$, where D is the diffusion coefficient. For natural convection driven by concurrent temperature and concentration gradients the general form of Grashof number is:

$$Gr_L = \frac{g(\Delta\rho/\rho)L^3}{\nu^2} = \frac{g(\rho_\infty - \rho_s)L^3}{\rho\nu^2}. \tag{1}$$

Here g is the gravity, L the characteristic dimension of the problem, $\rho = (\rho_s + \rho_\infty)/2$ the average density across the boundary layer and $\Delta\rho/\rho$ is the density change across the boundary layer (which, for a fuel cell cathode, will depend on both the temperature and concentration changes across the boundary layer). As a reasonable approximation, an air breathing fuel cell cathode surface can be treated as a heated horizontal plate. The commonly used formula for heat transfer above a heated horizontal plate is [18]:

$$\overline{Nu_L} = 0.54(Gr_L Pr)^{1/4}, \quad 10^4 \le Gr_L Pr \le 10^7 \tag{2}$$

Based on heat and mass transfer analogy, the mass transfer relationship is:

$$\overline{Sh_L} = 0.54(Gr_L Sc)^{1/4}, \quad 10^4 \le Gr_L Sc \le 10^7 \tag{3}$$

The heat transfer coefficient is therefore:

$$\bar{h}_{\text{T}} = \frac{\overline{Nu_L}k}{L} = 0.54k\left(\frac{2g}{\nu\alpha}\frac{\Delta\rho}{\rho}\right)^{1/4} L^{-(1/4)} \tag{4}$$

And the oxygen and water vapor mass transfer coefficients are:

$$h_{\text{O}_2} = \frac{\overline{Sh_L^{\text{O}_2}}D_{\text{O}_2,\text{air}}}{L_a} = 0.54D_{\text{O}_2,\text{air}}^{3/4}\left(\frac{\Delta\rho}{\rho}\frac{2g}{\nu}\right)^{1/4} L_a^{-(1/4)} \tag{5}$$

$$h_{\text{H}_2\text{O}} = \frac{\overline{Sh_L^{\text{H}_2\text{O}}}D_{\text{H}_2\text{O},\text{air}}}{L_a} = 0.54D_{\text{H}_2\text{O},\text{air}}^{3/4}\left(\frac{\Delta\rho}{\rho}\frac{2g}{\nu}\right)^{1/4} L_a^{-(1/4)} \tag{6}$$

Note that for the fuel cell cathode model, when calculating the heat transfer number, the characteristic length corresponds to the entire length of one edge of the fuel cell device (which we designate by L). In contrast, the appropriate characteristic length involved in H_2O and O_2 mass transfer is taken as the square root of the cathode active area (which we designate by L_a).

Accurate fuel cell thermal modeling requires radiation to be included in the analysis. At high current densities (when the cathode surface reaches 70–80 °C), radiation accounts for 30% of the total heat flux from the fuel cell. Failure to account for radiation heat transfer leads to large discrepancies between the calculated and experimentally measured fuel cell heat balance. Modifying Eq. (4) to account for radiation yields:

$$\begin{aligned} h_{\text{T}} &= \bar{h}_{\text{T}} + h_{\text{T,RAD}} \\ &= \bar{h}_{\text{T}} + 2\varepsilon_{\text{plate}}\sigma_{\text{boltz}}(T_{\text{GDL}}^2 + T_{\text{AMB}}^2)(T_{\text{GDL}} + T_{\text{AMB}}) \end{aligned} \tag{7}$$

where h_{T} is the modified heat transfer number, $h_{\text{T,RAD}}$ accounts for radiative heat transfer, $\varepsilon_{\text{plate}}$ the plate emissivity of the cathode and σ_{boltz} is the Stephan–Boltzmann constant. The factor of two accounts for radiation heat transfer from both sides of the device.

3. Model development

3.1. Model scope and assumptions

The air breathing fuel cell model developed in this paper is a simple, one-dimensional, steady state, cathode only fuel cell

model. A one-dimensional free-convection model is especially well suited to describing the situation at a planar air breathing fuel cell cathode because there are no directional forced flows. The following list details the major assumptions used in developing this model:

- One-dimensional transport;
- Steady state conditions;
- Single phase flow (only water vapor transport is considered);
- The effects of liquid water accumulation (flooding) are not treated;
- Dead-ended anode;
- Dry (zero humidity) hydrogen supply;
- No water accumulation in the anode;
- No net water transport through the membrane (a ramification of flux balance with dead-ended anode assuming no liquid water accumulation in anode);
- Water activity is uniform across the membrane and is in equilibrium with the water vapor activity at the cathode catalyst layer;
- The cathode catalyst layer is infinitely thin (treated as a surface).

A major limitation of the current model is its failure to account for liquid water flooding. Although the model tracks liquid water accumulation, the model does not evaluate liquid water transport. Also, the model does not take into account the deleterious effects of flooding on fuel cell performance. Experimental research suggests that flooding is a significant problem in air breathing fuel cells [21]. Therefore, a major emphasis of future work will be to implement liquid water transport and flooding effects into the model.

Since water activity is assumed uniform within the membrane and no net water transport is permitted to cross it, we assume that the conductivity of the membrane is set by the temperature and water vapor activity at the cathode catalyst interface. This simplification allows us to narrow our model domain so that only transport processes occurring between the cathode catalyst interface and quiescent ambient air above the cathode surface are considered. This region is further broken down into two domains: (1) the cathode gas diffusion layer (GDL) and (2) the cathode natural convection boundary layer. We apply diffusion governing equations to describe the transport processes within the GDL and convection governing equations to describe the transport processes in the natural convection boundary layer just above the cathode surface. The complete model space is diagrammed schematically in Fig. 1. Although the equations presented in this model development are based on concentration, for gas phase species at low pressure, the ideal gas law can be used to convert between concentration and pressure as $P_i = RTc_i$, where P_i is the partial pressure of species i, R the ideal gas constant, T the temperature and c_i is the concentration of species i.

3.2. Model domain and governing equations

Space does not permit full discussion of the model development here. Instead, Table 1 summarizes the set of equations

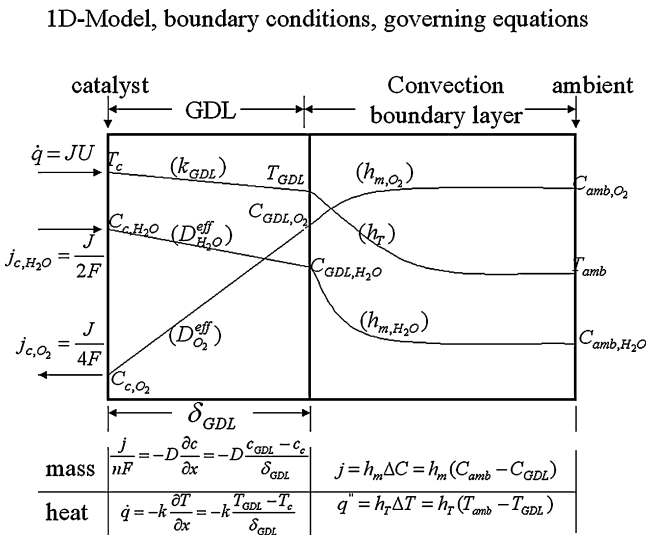

Fig. 1. Schematic diagram of the model domain, governing equations and relevant parameters. Shown are traces of temperature, water concentration and oxygen concentration. The relevant flux constant is shown in parentheses by each curve.

used in the model formulation while Table 2 summarizes the nomenclature. Model solution is accomplished using an iterative approach. The boundary values above the cathode natural convection boundary layer (T_{AMB} and $c_{i,AMB}$) are set by the ambient conditions (ambient temperature, pressure and rela-

Table 1
Summary of equations used to formulate the air breathing fuel cell combined convection and heat transfer cathode model

Cathode GDL domain governing equations

$$j = -n_i F D_i^{\text{eff}} \frac{\mathrm{d}c_i}{\mathrm{d}x} = -n_i F D_i^{\text{eff}} \frac{c_{i,\text{GDL}} - c_{i,\text{c}}}{\delta_{\text{GDL}}}, \quad \text{where } D_i^{\text{eff}} = \frac{\varepsilon}{\tau} D_{i,\text{air}} \tag{8}$$

$$\dot{q} = -k_{\text{GDL}} \frac{\mathrm{d}T}{\mathrm{d}x} = -k_{\text{GDL}} \frac{T_{\text{GDL}} - T_{\text{c}}}{\delta_{\text{GDL}}} \tag{9}$$

Natural convection boundary layer governing equations

$$j = h_i \, \Delta c_i = h_i(c_{i,\text{AMB}} - c_{i,\text{GDL}}) \tag{10}$$

$$\dot{q} = h_{\text{T}} \, \Delta T = h_{\text{T}}(T_{\text{AMB}} - T_{\text{GDL}}) \tag{11}$$

Fuel cell heat flux

$$\dot{q} = j \left[(E_{\text{ocv}} - V) - \left(\frac{T \, \Delta s_{\text{RXN,H}_2\text{O}_{(\text{g})}}}{2F} \right) + \left(\frac{x_{\text{H}_2\text{O},l} \, \Delta H_{\text{cond}}}{2F} \right) \right] \tag{12}$$

Fuel cell polarization model

$$V = E_{\text{ocv}} - \eta_{\text{kinetic}} - \eta_{\text{iR}} \tag{13}$$

$$E_{\text{ocv}} = E^0_{303\,\text{K}} - \left[\frac{RT_{\text{c}}}{2F} \right] \ln \left[\frac{c_{\text{O}_2,\text{AMB}}}{c_{\text{O}_2,\text{c}}} \right] \tag{14}$$

In refs. [24,25]

$$\eta_{\text{iR}} = iR = jA_{\text{cell}}R = jA_{\text{cell}}[R_{\text{elec}} + R_{\text{mem}}], \quad \text{where } R_{\text{mem}} = \left[\frac{\delta_{\text{mem}}}{A_{\text{cell}}\sigma_{a,T}} \right] \text{ and } \sigma_{a,T} = [3.46a^3 + 0.0161a^2 + 1.45a - 0.175] \times [\mathrm{e}^{1268((1/303)-(1/T))}] \tag{15}$$

In ref. [26]

$$\eta_{\text{kinetic}} = \frac{RT_{\text{c}}}{2\alpha F} \ln \left[\frac{jc_{\text{O}_2,\text{AMB}}}{j^0_{303\,\text{K}}[\mathrm{e}^{\Delta G_{\text{act}}/R((1/303)-(1/T))}]c_{\text{O}_2,\text{c}}} \right] \tag{16}$$

Table 2
Summary of model equation symbols and nomenclature

Symbol and description	Units
Constants	
Universal gas constant, R	8.315 J mol^{-1} K
Faraday's constant, F	96,500 C mol^{-1}
Gravity, g	9.8 m s^{-2}
Stephan–Boltzmann constant, σ_{boltz}	9.67×10^{-8} W m^{-2} K^4
Ambient conditions	
Ambient pressure, P	101000 pA
Ambient relative humidity, RH_{AMB}	As specified (%)
Ambient temperature, T_{AMB}	As specified (°C)
Model terms	
Effective diffusivity, D_i^{eff}	m^2 s^{-1}
GDL porosity, ε	Dimensionless
GDL tortuosity, τ	Dimensionless
Binary diffusivity of species i in air, $D_{i,air}$	m^2 s^{-1}
Catalysts layer temperature, T_c	K
GDL interface temperature, T_{GDL}	K
GDL thickness, δ_{GDL}	M
Thermal conductivity of the GDL, k_{GDL}	W m^{-1} K
Concentration of species i in ambient, $c_{i,AMB}$	mol m^{-3}
Concentration of species i in GDL, $c_{i,GDL}$	mol m^{-3}
Concentration of species i in catalyst layer, $c_{i,c}$	mol m^{-3}
Entropy of fuel cell reaction, $\Delta s_{RXN,H_2O\,(g)}$	−44.43 J mol^{-1} K
Heat of water condensation, ΔH_{cond}	40 kJ mol^{-1}
Fraction of liquid water, $x_{H_2O,l}$	Dimensionless
Reference reversible fuel cell voltage, $E^0_{303\,K}$	V
Lumped cell electrical resistance, R_{elec}	Ω
Cell membrane resistance, R_{mem}	Ω
Cell active area, A_{cell}	m^2
Nafion thickness, δ_{mem}	m
Water vapor activity, a	Dimensionless
Charge transfer coefficient, α	Dimensionless
Reference exchange current density	$j^0_{303\,K}$
Exchange current density activation energy, ΔG_{act}	kJ mol^{-1}

tive humidity). At the catalyst layer, the boundary conditions (j, T_c, $c_{i,c}$) are provided as *guesses* by the solver program for a given input voltage (V). Based on these initial guesses, the solver algorithm uses Eqs. (8)–(11) (in Table 1) to re-compute ambient conditions. The magnitude and direction of the error between the computed ambient conditions (based on the guessed inputs for the catalyst layer boundary conditions) and the fixed ambient conditions is then used to refine the guess for the catalyst layer boundary conditions and the solution procedure is repeated. Iterative refinement proceeds until the errors between the real and calculated ambient conditions drop below a minimum threshold (the error between the input and calculated cell voltage is minimized simultaneously as well, using Eqs. (13)–(16)). Once acceptable solutions have been calculated at a given input voltage, the voltage is stepped to a new value and the solution algorithm is repeated. In this manner, full model data for a complete IV curve is acquired. The iterative guess refinement solver algorithm used in this model is based on a form of the generalized reduced gradient optimization method that was developed by Leon Lasdon, of the University of Texas at Austin, and Allan Waren, of Cleveland State University for optimization of non-linear problems [19].

Table 3
Example model output from air breathing fuel cell simulation at ambient conditions = 10 °C, 40% RH

IV		Fuel cell overpotentials				Catalyst surface				GDL surface				Heat and mass transfer		
V_{cell} (V)	J (mA cm^{-2})	E_{ocv} (V)	$\eta_{kinetic}$ (V)	η_{iR} (V)	R (mΩ)	T_c (°C)	$P_{O_2,c}$ (atm)	$P_{H_2O,c}$ (atm)	RH_c (%)	$x_{H_2O(l)}$	T_{GDL} (°C)	$P_{O_2,GDL}$ (atm)	$P_{H_2O,GDL}$ (atm)	RH_{GDL} (%)	Nu_L	$Sh_L^{O_2}$	$Sh_L^{H_2O}$
1.23	0	1.23	0.00	0.00	90.00	10.0	0.210	0.006	45.0	0.00	10.0	0.210	0.006	45.0	NA	NA	NA
0.80	79	1.23	0.40	0.02	26.91	15.9	0.194	0.018	100.0	0.52	15.8	0.200	0.014	78.7	12.4	6.6	6.2
0.78	113	1.23	0.42	0.03	26.32	18.6	0.188	0.022	100.0	0.56	18.4	0.196	0.016	76.1	13.5	7.1	6.8
0.75	150	1.23	0.44	0.03	25.70	21.6	0.182	0.026	100.0	0.57	21.3	0.192	0.019	73.7	14.4	7.6	7.2
0.73	192	1.23	0.46	0.04	25.05	25.0	0.175	0.031	100.0	0.56	24.6	0.188	0.022	71.5	15.2	8.1	7.7
0.70	239	1.23	0.47	0.05	24.39	28.6	0.168	0.039	100.0	0.53	28.2	0.184	0.026	69.5	15.9	8.5	8.1
0.68	288	1.23	0.49	0.06	23.76	32.4	0.160	0.048	100.0	0.50	31.9	0.180	0.032	67.9	16.6	8.9	8.4
0.65	339	1.23	0.50	0.07	23.16	36.3	0.151	0.059	100.0	0.45	35.7	0.175	0.038	66.5	17.1	9.2	8.7
0.63	392	1.22	0.52	0.08	22.59	40.3	0.143	0.074	100.0	0.40	39.6	0.171	0.046	65.3	17.6	9.5	9.0
0.60	447	1.22	0.53	0.09	22.06	44.4	0.134	0.091	100.0	0.33	43.5	0.166	0.056	64.3	18.1	9.8	9.3
0.58	503	1.22	0.55	0.10	21.57	48.4	0.124	0.111	100.0	0.26	47.4	0.161	0.067	63.5	18.5	10.1	9.5
0.55	560	1.22	0.56	0.11	21.12	52.4	0.114	0.135	100.0	0.19	51.2	0.156	0.080	62.8	18.9	10.3	9.8
0.50	683	1.22	0.59	0.12	20.30	60.5	0.093	0.198	100.0	0.01	59.1	0.146	0.115	61.7	19.7	10.8	10.2
0.45	731	1.22	0.61	0.16	24.22	66.3	0.084	0.215	83.0	0.00	64.7	0.141	0.123	51.1	20.0	11.0	10.4
0.40	756	1.22	0.62	0.20	28.83	70.8	0.079	0.223	70.8	0.00	69.1	0.139	0.127	43.5	20.1	11.1	10.5
0.35	772	1.21	0.63	0.24	34.19	74.8	0.076	0.229	61.3	0.00	72.9	0.137	0.130	37.7	20.3	11.2	10.6
0.30	778	1.21	0.63	0.28	40.04	78.2	0.074	0.232	54.1	0.00	76.1	0.137	0.131	33.2	20.4	11.3	10.7
0.25	778	1.21	0.64	0.32	46.37	81.1	0.073	0.233	48.3	0.00	78.9	0.136	0.131	29.7	20.4	11.3	10.8
0.20	774	1.21	0.64	0.37	53.19	83.6	0.073	0.233	43.6	0.00	81.4	0.136	0.131	26.8	20.5	11.4	10.8

All model parameters are as listed in Table 2.

Once a complete solution has been generated, model outputs include calculated IV data, iR and kinetic overpotentials, values for the temperature and species concentrations at the catalyst and GDL surfaces, and the condensed water fraction. In analyzing the model results, we find that both water concentration and relative humidity are useful. To convert between RH and water concentration, a standard polynomial expression for the saturation pressure of water (P_{SAT,H_2O}) is used [20], yielding:

$$\mathrm{RH} = \frac{P_{H_2O}}{P_{SAT,H_2O}} \times 100\% = \frac{R \times T \times c_{H_2O}}{10^{(-2.1794+0.02953T-9.1837\times10^{-5}T^2+1.4454\times10^{-7}T^3)}} \times 100\% \quad (17)$$

Under certain conditions, the model predicts water vapor supersaturation (RH > 100%) at the cathode catalyst layer. Under these conditions, liquid water condensation would occur. Our model accounts for liquid water condensation with a liquid water faction term, $x_{H_2O,l}$.

$$x_{H_2O,l} = \frac{\mathrm{RH}\,(\%) - 100}{100} \quad (\text{for RH} > 100\%) \quad (18)$$

The liquid water fraction term represents the fraction of water produced at the cathode that is condensed as liquid water. If RH < 100%, then $x_{H_2O,l} = 0$. Note that this term appears in the fuel cell heat flux Eq. (12) to account for the heat released upon liquid water condensation.

Example output of the model for an air breathing fuel cell operating at ambient conditions of 10 °C and 40% RH is provided in Table 3. As shown in the table, Nuesselt numbers obtained from our model are typically in the order of 10–20 while Sherwood numbers are typically in the order of 6–12. These large values indicate the relative dominance of convective (rather than diffusive) heat and mass transport above the cathode surface.

4. Model validation and discussion

4.1. Model validation

In this section, the model is validated against experimental data over a range of ambient conditions in order to gauge the extent of its applicability. This comparison is made against recently described experimental measurements from a 3 cm × 3 cm air breathing fuel cell device [21]. The baseline properties used by the model are listed in Table 4. Fixed inputs and cell properties were obtained from the literature or directly from the geometry of the experimental cell. Only the four properties highlighted in gray (k_{GDL}, R_{elec}, $j^0_{303\,K}$ and α) were used as free-floating fitting parameters. A single set of these fitting values was used to fit all measurements and conditions; these best-fit values are documented in Table 4. Starting from this baseline, the model was validated against measurements made at ambient temperatures of 10, 20 and 30 °C (in all cases at 40% RH). A comparison between the experimental and results is provided in Fig. 3a–d.

As Fig. 2 indicates, the model nicely predicts the relative trends in air breathing fuel cell behavior as a function of ambient temperature. The model recovers the experimentally observed decrease in performance with increasing ambient temperature due to fuel cell overheating and consequent membrane dry-out. This dry-out phenomenon is indicated by the results in Fig. 2c and d, which show the effect of cell self-heating (Fig. 2d) and the resulting increase in fuel cell resistance above a critical current density due to membrane dry-out (Fig. 2c). In particular, note how the model effectively captures the rapid increases in cell resistance and temperature that occur due to the non-linear effects of membrane dry-out at high current densities. A traditional non-coupled or isothermal fuel cell model would not capture these non-linearities. The model also captures the general trends for water accumulation, although not the proper magnitude, as shown in Fig. 2b. The model's superficial treatment of liquid water likely explains this quantitative discrepancy. As discussed in Section 3.1, the model assumes that there is no water transport across the membrane, and hence no accumulation of liquid water in the anode. However, this assumption is problematic since anode liquid water accumulation is observed experimentally. Experimentally, water condenses in the dead-ended anode due to the existence of temperature gradients between catalyst layer and anode gas channel walls (which our model neglects). Due to this temperature gradient, under conditions where cathode is close to saturation, hydrogen gas becomes supersaturated at the walls of the anode gas channels, leading to condensation. Because the anode is dead-ended, any water that condenses in the anode will simply accumulate in the anode compartment. This additional water sink likely explains why experimental measurements of liquid water accumulation are greater than the model predictions.

As shown in Table 3, in addition to predicting overall IV behavior, the model provides detailed results for temperature and species concentrations at both the catalyst and GDL surfaces. Recently, we have experimentally investigated the actual temperature and species concentrations at the GDL surface of an air breathing fuel cell by employing microscale oxygen, relative humidity and temperature sensors [22]. By comparing the experimental and model results for GDL surface temperature and species concentration as a function of current density, it is therefore possible to further authenticate the physical correctness of our model. An example of this comparison is provided in Fig. 3 for an air breathing fuel cell operated at ambient conditions of 21 °C, 35% RH.

Fig. 4 shows that most of the experimentally observed trends are also reflected in the model predictions. The temperature fit between the experimental and model data is especially good, indicating that the heat transfer portion of our model is accurate. The model overestimates both P_{O_2} and P_{H_2O}. The model's overestimate for P_{H_2O} is likely due to the assumption of zero water transport to the anode. As discussed earlier, we experimentally observe that some of the water produced by the cell transports to the anode. This anode water sink therefore reduces the water concentration at the cathode. The approximate two-fold discrepancy

Table 4
Properties (and their values) used in the base case air breathing fuel cell model

Property	Value
Constants	
Universal gas constant, R	8.315 J/mol*K
Faraday's constant, F	96,500 C/mol
Gravity, g	9.8 m/s^2
Stephan-Boltzmann constant, σ_{boltz}	$9.67x10^{-8}$ W/m^2*K^4
Ambient conditions	
Ambient pressure, P	101000 pA
Ambient relative humidity, RH_{AMB}	As specified (%)
Ambient temperature, T_{AMB}	As specified (°C)
Fixed Inputs	
Plate emissivity, ε_{plate}	0.90
Thermal conductivity of air, k_{air}	0.027 W/m*K
Binary diffusivity of O_2 in air, $D_{O2,air}$	$2.1x10^{-5}$ m^2/s
Binary diffusivity of H_2O in air, $D_{H2O,air}$	$2.6x10^{-5}$ m^2/s
Reference reversible fuel cell voltage, E^0_{303K}	1.23 V
Entropy of fuel cell reaction, $\Delta s_{RXN,H2O(g)}$	-44.43 J/mol*K
Heat of water condensation, ΔH_{cond}	40 kJ/mol
Cell Properties	
Characteristic dimension of fuel cell device (square), L	0.07 m
Length of active cell side (square), L_a	0.03 m
Cell active area, A_{cell}	0.0009 m^2
Nafion thickness, δ_{mem}	$5.2x10^{-5}$ m
GDL thickness, δ_{GDL}	$3.0x10^{-4}$ m
GDL porosity, ε	0.40
GDL tortuosity, τ	3.0
Exchange current density activation energy, ΔG_{act}	50 kJ/mol
Fitting parameters	
GDL thermal conductivity, k_{GDL}	10 W/m*K [27]
Lumped cell electrical resistance, R_{elec}	0.012 Ω [21]
Reference exchange current density, j^0_{303K}	$5x10^{-5}$ A/cm^2
Charge transfer coefficient, α	0.28 [28,29]

Cell geometry and MEA properties are based on the experimental 3 cm × 3 cm air breathing fuel cell described in ref. [21]. Also see refs. [27–29].

between the experimental and model P_{H_2O} readings indicates that as much as half of the generated water may transport to the anode. This is consistent with the results in Fig. 2b, where the model values for accumulated water also deviate by a factor of approximately two.

The largest apparent discrepancy between the experimental and model results arises in the humidity data, with the model dramatically overestimating GDL humidity (although adequately capturing the shape of the humidity versus current density curve). The large discrepancy between the model and measurements of RH is a direct result of the model's overprediction of P_{H_2O}. Because RH is linearly proportional to P_{H_2O}, the model's overestimate of P_{H_2O} (by approximately a factor of two), leads to an overestimate in RH (also by approximately a factor of two).

Overall, the model capturse the major trends associated with cell temperature, dry out and cell-to-atmosphere mass transport, while falling short of giving accurate humidity values immediately above the fuel cell cathode. We are currently refining our model further to account for flooding and water transport to the anode.

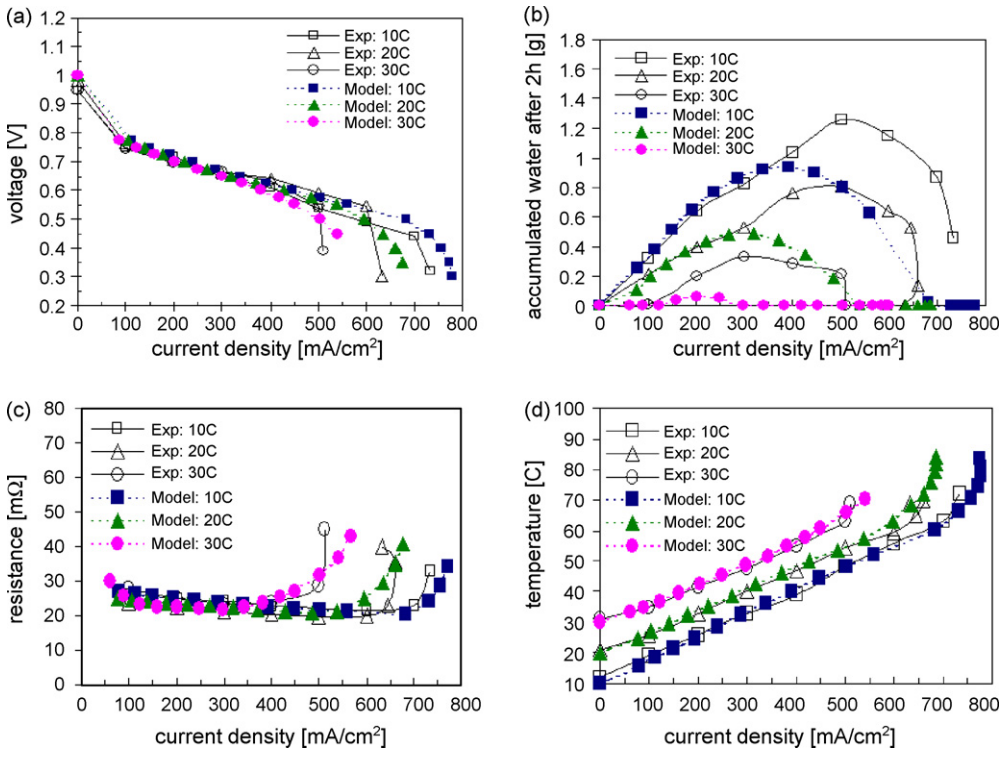

Fig. 2. Comparison of experimental and model results for an air breathing fuel cell operated at ambient temperatures of 10, 20 and 30 °C, 40% relative humidity. (a) Polarization curves, (b) accumulated water after 2 h of steady state operation at a range of current densities, (c) cell resistance as a function of current density and (d) GDL surface temperature as a function of current density.

4.2. Scenario modeling

Having validated the model against experimental air breathing fuel cell data, we now use the model to investigate several scenarios. Specifically, we examine the effect of GDL thickness, GDL thermal conductivity and increasing heat/mass transfer with the addition of forced convection. In all scenarios, ambient conditions of 20 °C and 40% RH are chosen to best reflect the likely conditions encountered by an actual air breathing fuel cell device.

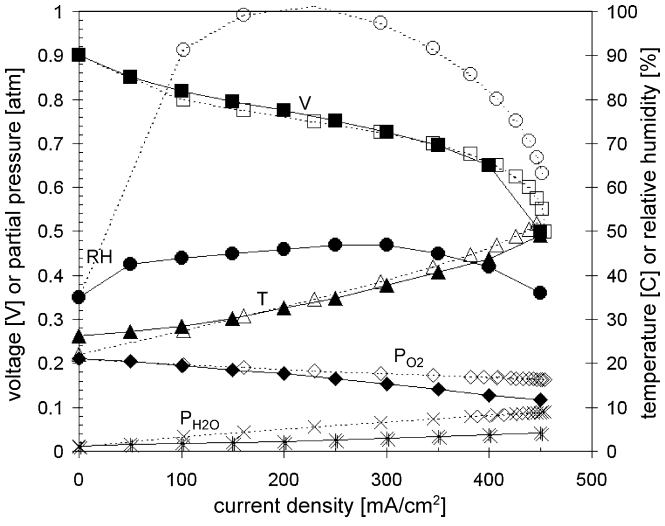

Fig. 3. Comparison of experimental (closed symbols) and model (open symbols) results for GDL surface relative humidity, temperature and species concentrations as a function of current density. The model and experimental IV curves are also shown for comparison.

4.2.1. Effect of GDL thickness

Fig. 4 provides a parametric analysis of how variations in the GDL thickness affect modeled air breathing fuel cell behavior. Inspection of Fig. 4 reveals that the model predicts an optimum in fuel cell performance for a GDL thickness of approximately 500 μm. Thicker or thinner GDLs result in decreased performance. (Please note that this model investigation does not take the electrical resistance of the GDL into account; these electrical resistance differences may be important when comparing very thick versus very thin GDLs.) Interestingly, the real GDL thickness used in current air breathing fuel cells (∼300 μm, indicated by the base case) is slightly thinner than the predicted model optimum. The reason for a model optimum is uncovered from careful analysis of the complete model data. For the thinnest GDL, water is rejected too easily from the cathode, leading to premature membrane dry-out. For the thickest GDL, the thermal resistance of the GDL itself starts to become an important factor, causing a more rapid temperature rise at the catalyst layer and leading to dry-out. This temperature effect is observable in the increased slope of the curves in Fig. 4d with increasing GDL thickness. This scenario indicates that GDL thickness optimization involves a delicate balance between the heat and water transport rates within the fuel cell. This issue of matching the heat rejection and water rejection requirements *is one of the most important considerations* in optimizing air breathing fuel cell performance.

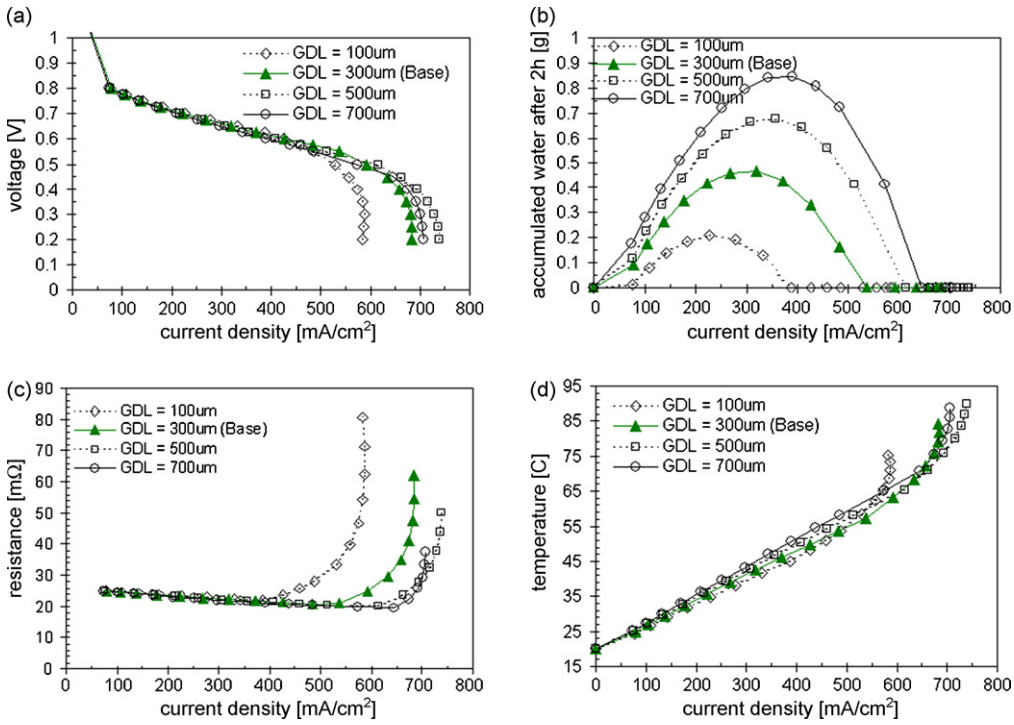

Fig. 4. The effect of GDL thickness on modeled air breathing fuel cell behavior. The base case (GDL thickness = 300 μm) is indicated with solid triangles. (a) Polarization curves, (b) accumulated water after 2 h of steady state operation at a range of current densities, (c) cell resistance as a function of current density and (d) catalyst/membrane temperature as a function of current density. Ambient conditions are 20 °C, 40% RH. The other parameters used in this model simulation are detailed in Table 4.

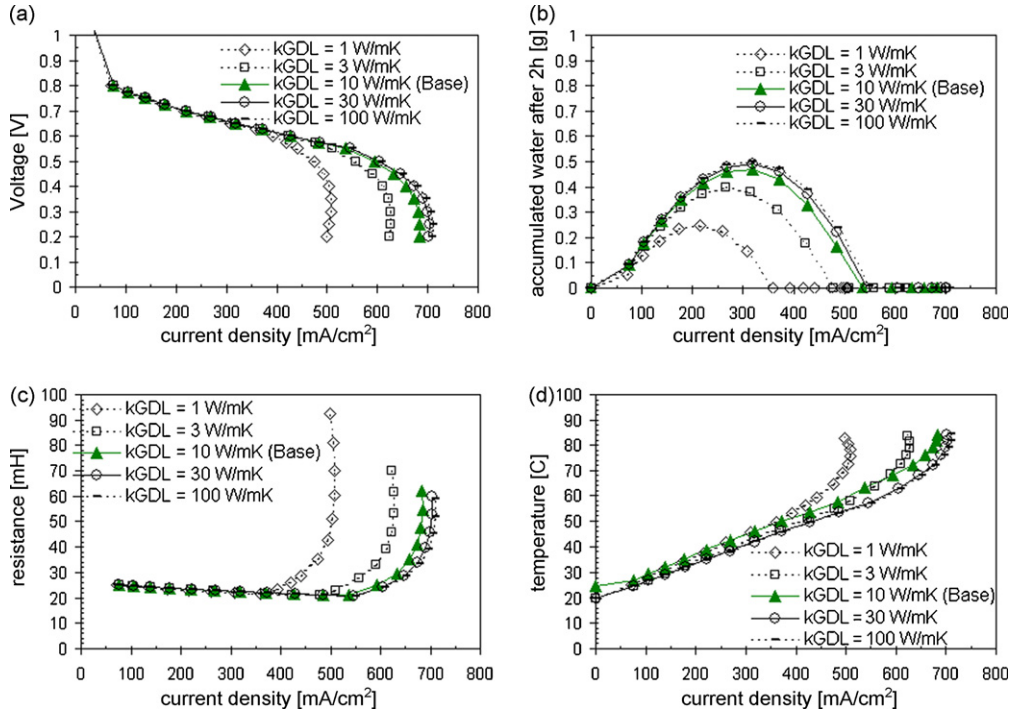

Fig. 5. The effect of GDL thermal conductivity (k_{GDL}) on modeled air breathing fuel cell behavior. The base case (k_{GDL} = 10 W mK^{-1} is indicated with solid triangles. (a) Polarization curves, (b) accumulated water after 2 h of steady state operation at a range of current densities, (c) cell resistance as a function of current density and (d) catalyst/membrane temperature as a function of current density. Ambient conditions are 20 °C, 40% RH. The other parameters used in this model simulation are detailed in Table 4.

4.2.2. Effect of GDL thermal conductivity

Fig. 5 provides a parametric analysis of how variations in the GDL thermal conductivity affect modeled air breathing fuel cell behavior. With increasing GDL thermal conductivity, air breathing fuel cell performance first increases, and then saturates for thermal conductivity values greater than 30 W mK^{-1}. At first, performance is improved by increasing k_{GDL}, which improves heat rejection from the cathode and delays the onset of membrane dry-out. However, the saturation behavior for $k_{GDL} > 30$ W mK^{-1} indicates that for highly conductive GDLs, the thermal bottleneck shifts from the GDL to the convection boundary layer. Thus, heat advection away from the GDL by natural convection in the free air above the cathode becomes the new rate-controlling process. As with the previous scenario, it is clear that fuel cell performance is improved by increasing the heat rejection capabilities of the cell. By rejecting greater amounts of heat, the onset of dry-out can be delayed to higher and higher current densities. *Our model suggests that it is this membrane dry-out process, and not oxygen depletion, that limits the performance of air breathing fuel cells*.

In order to operate an air breathing fuel cell at extremely high power densities, significantly greater heat rejection capabilities than those obtainable from natural convection are required. For example, a fuel cell operating at 0.5 V and 2.0 A cm^{-2} (corresponding to a power density of 1 W cm^{-2}) would produce approximately 2 W cm^{-2} of heat. To maintain a steady state catalyst temperature of 70 °C (approximately the maximum sustainable temperature before the onset of thermal runaway) would require a heat transfer number of approximately 400 W m^{-2} K (assuming $T_{AMB} = 20$ °C). Advection of this heat load from the cathode surface requires a Nusselt number of approximately 1000. Such a Nusselt number is certainly not obtainable with natural convection and would correspond to extremely vigorous forced convection. Rather than relying on convection, one interesting alternative would be to remove this heat via conduction to a heat sink. Such thermal engineering possibilities will be an interesting subject of future experimental and modeling activity.

4.2.3. Effect of forced convection

To reinforce the conclusions drawn from the previous scenario, this final scenario examines what type of performance benefits may be possible if forced convection is introduced into the fuel cell model. As shown in Table 3, the Nusslet/Sherwood numbers obtained due to natural convection above the fuel cell cathode are in the order of 5–20. This range is on the same order of magnitude as naturally occurring air currents in an indoor building. In contrast, a light (but perceptible) breeze would yield Nusselt/Sherwood numbers of 30–50 while vigorous forced air flow can yield Nusselt/Sherwood numbers of 100–1000. Since even a light breeze yields higher transport numbers than those due to natural convection, it is interesting to investigate what effect this might have on air breathing fuel cell performance. This analysis is provided in Fig. 6, which summarizes the changes in model fuel cell behavior due to the superposition of an additional Nusselt/Sherwood term accounting for varying degrees of forced convection. Increases of 10, 30, 100 and 300 to the Nusselt/Sherewood numbers are considered. As with the previ-

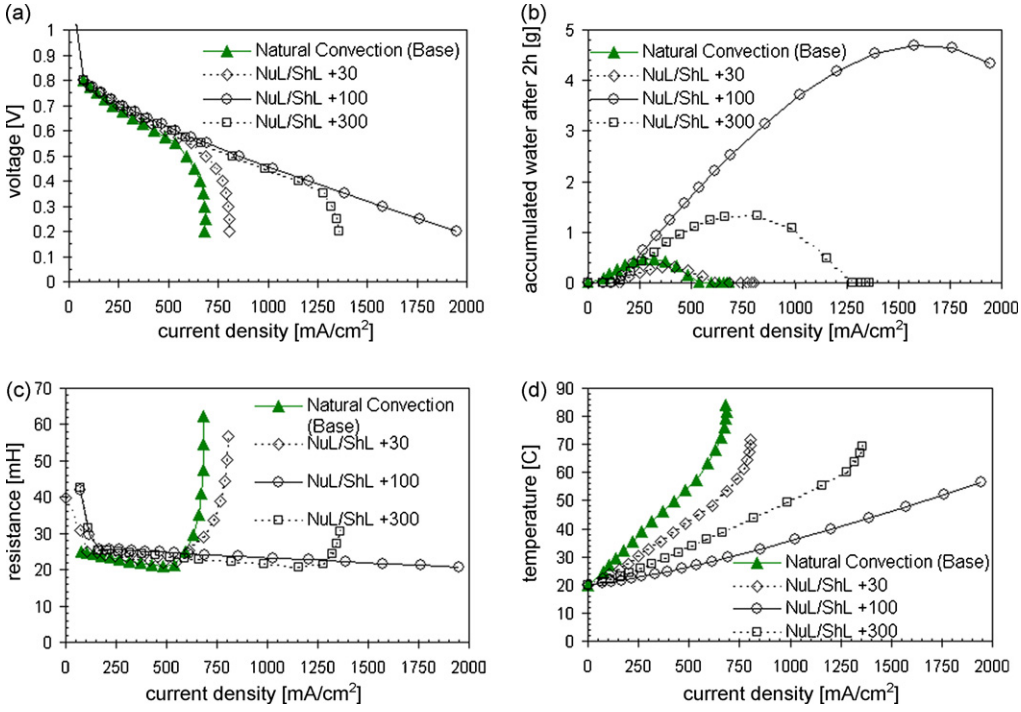

Fig. 6. The effect of forced convection on modeled air breathing fuel cell behavior. The base case (natural convection only) is indicated with solid triangles. (a) Polarization curves, (b) accumulated water after 2 h of steady state operation at a range of current densities, (c) cell resistance as a function of current density and (d) catalyst/membrane temperature as a function of current density. Ambient conditions are 20 °C, 40% RH. The other parameters used in this model simulation are detailed in Table 4.

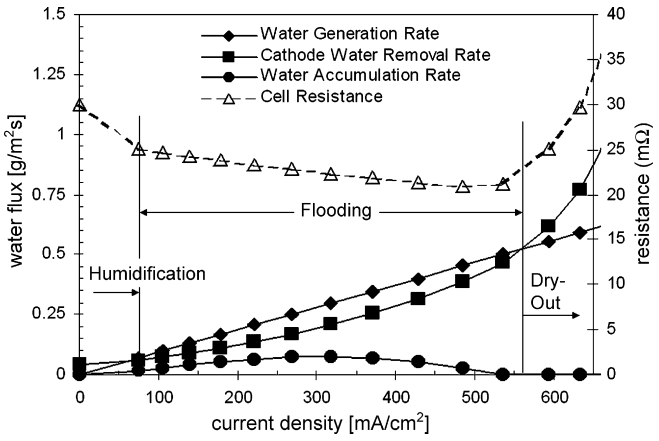

Fig. 7. Water balance in an air breathing fuel cell. The properties plotted in this graph were obtained from model simulation of an air breathing fuel cell at 20 °C, 40% RH. All other properties are as listed in Table 4. Water generation increases linearly with increasing current density. Water removal increases exponentially with increasing current density (due to cell self-heating). The competition between water generation and removal leads to three characteristic operating regions: humidification (at low current density), flooding (at intermediate current densities) and dry-out (at high current density).

ous scenarios, all other parameters remain fixed as specified by the base case properties listed in Table 4.

As indicated by Fig. 6, forced convection dramatically improves fuel cell performance by increasing heat transfer (through improved advection from the cathode surface), thus delaying the onset of membrane dry-out. For the highest forced convection rate ($Nu_L/Sh_L \sim 300$), the cell never reaches the critical temperature for dry-out and performance is limited only by the iR losses. However, as shown by the data in Fig. 6b, liquid water accumulation also increases with increasing forced convection, indicating that these cells, in reality, would face massive flooding problems and never achieve the predicted model performance. The failure of our model to account for flooding limits our ability to attempt further quantitative analysis in this scenario. However, these results provide an important conclusion about the coupling between thermal and water management in air breathing fuel cells; improved thermal rejection is desirable because it delays the onset of dry-out, but it also leads to increased liquid water accumulation (because exponentially less water can be removed at lower cell temperatures). Thus, the desire to increase heat rejection often conflicts with the desire to avoid flooding. This "Goldilocks" problem of air breathing fuel cell design will be further discussed in the following section (Fig. 7).

4.2.4. Water balance in air breathing fuel cells

As indicated above, the difficulty of reconciling heat and water management often leads to flooding or dry-out problems in air breathing fuel cells. Flooding is most easily tracked by monitoring accumulated water (a signal of flooding) while dry-out can be detected by monitoring cell resistance (a dramatic increase in cell resistance indicates membrane dry-out). For example, the experimental and model results in Fig. 2b and c show the characteristic hallmarks of both flooding (at intermediate current densities) and dry-out (at elevated current densities). Not surprisingly, operation at higher ambient temperature reduces the window of flooding and expedites dry-out. Our model can be used to understand the factors that control flooding and dry-out. This analysis is presented in Fig. 7, which plots cell resistance and water accumulation (our signatures for flooding and dry-out) along with the principle water flux curves responsible for the water balance in the air breathing fuel cell.

The changing water balance dynamics in the fuel cell lead to the three regimes indicated on the figure: self-humidification at low current density, saturation and flooding at moderate current densities and dry-out at high current densities. Ideal water balance is only achieved at two operating points: (1) at the transition between the self-humidification and flooding regimes and (2) at the transition between the flooding and membrane dry out regimes. The complex interplay between heat and water balance, which leads to these transition points, can be understood by carefully examining the water flux curves. The regime transitions are controlled by the competition between the water generation rate and the maximum water removal rate. The generated water flux versus current density curve is linear with slope = $1/2F$. The maximum water flux that can be removed from the cathode increases exponentially with increasing current density due to the coupling between current density and cathode surface temperature. The cathode surface temperature increases roughly linearly with increasing current density (see, for example; Fig. 2d), but this leads to an exponentially increasing water vapor saturation pressure at the cathode surface, and therefore leads to an exponential increase in the flux of water that can be removed from the cathode. Note that the curves intersect twice. At current densities below the first intersection, self-humidification occurs (as the two curves converge with increasing current density). Between these two intersections, the water flux generated by electrochemical reaction exceeds the maximum water removal rate, leading to membrane saturation and eventual flooding. At current densities above the second intersection, dry-out occurs (as the two curves diverge with increasing current density).

A change in the ambient conditions (ambient temperature or humidity) will cause the water flux removal curve to shift. For example, Fig. 8 shows the impact of increasing the ambient humidity on water balance. Increasing the ambient humidity causes the cathode water removal curve to shift downwards (a moisture ambient atmosphere decreases our ability to remove water from the cathode.) This shift expands the region of membrane saturation, intensifying flooding, but delaying the onset of dry-out. A change in ambient temperature causes similar effects.

4.2.5. Properties of the natural convection boundary layer

Because forced convection can dramatically impact air breathing fuel cell behavior, it is insightful to ask: how far does the natural convective boundary layer penetrate into the ambient air above the fuel cell cathode? The characteristic thickness of the natural convection boundary layer can be approximated from our model using the following simple relation:

$$\delta_{\text{conv}} \approx \frac{D}{h} \tag{19}$$

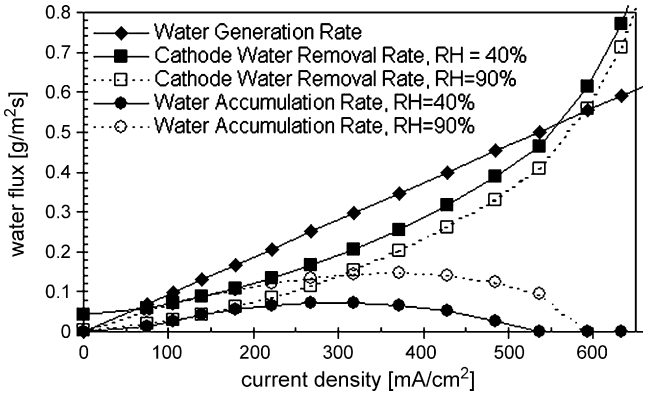

Fig. 8. Influence of ambient humidity on air breathing fuel cell water balance. Relative to the situation at 40% RH (closed symbols), increasing the ambient RH to 90% shifts the cathode water removal curve downwards and exacerbates liquid water accumulation (open symbols). Model simulation at $T_{AMB} = 20\,^{\circ}C$, all other properties as listed in Table 4.

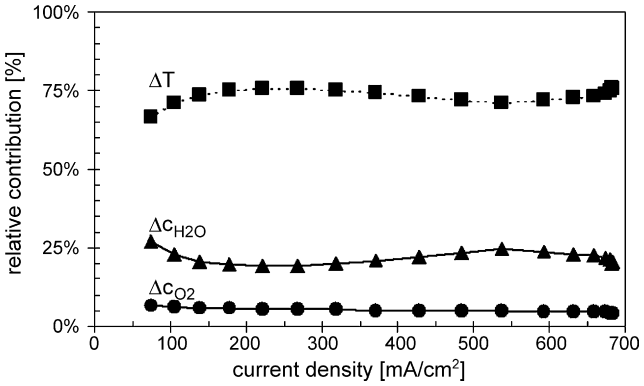

Fig. 9. Relative contribution of the thermal, oxygen, and water vapor gradients on the natural convection process at an air breathing fuel cell. Results are based on the standard model simulation at ambient conditions of 20 °C, 40% RH, all other properties as listed in Table 4.

The room temperature diffusivities for air and water (see Table 4) are $D_{O_2} = 2.1 \times 10^{-5}\,m^2/s$ and $D_{H_2O} = 2.6 \times 10^{-5}\,m^2/s$, respectively. The model-calculated mass transfer numbers for O_2 and H_2O are approximately $h_{O_2} = 0.006\,m/s$ and $h_{H_2O} = 0.007\,m/s$. Eq. (19) therefore yields an estimated thickness of the natural convection boundary layer of approximately 0.0035–0.0037 m = 3.5–3.7 mm. This is an order of magnitude larger than the thickness of the typical fuel cell GDL (~300 μm). This surprisingly large boundary layer thickness has recently been confirmed by spatially resolved experimental measurements of oxygen, water and temperature profiles above an air breathing fuel cell GDL [22]. The large thickness of the convective boundary layer is one of the key distinguishing characteristics of free-breathing fuel cells compared to forced-flow fuel cells. In a forced flow situations, the convective boundary layer thickness is greatly reduced (to the order of 30–100 μm), consistent with the one to two orders of magnitude increase in h.

Because the model considers coupled heat and mass transport, it is instructive to ask what fraction of the natural convection cathode mass transfer is driven by the thermal gradient, the water vapor gradient and the oxygen gradient, respectively. This separation can be accomplished via application of the Boussinesq approximation [23], which allows the relative contributions of ΔT, Δc_{O_2} and Δc_{H_2O} to $\Delta\rho/\rho$ to be isolated from one another (for small density variations). For a fuel cell cathode, assuming that density changes are only caused by gradients in temperature, water and oxygen, the Boussinesq approximation may be written as:

$$\frac{\Delta\rho}{\rho} = \beta^{T}(T_{GDL} - T_{AMB}) + \beta^{O_2}(c_{O_2,GDL} - c_{O_2,AMB}) + \beta^{H_2O}(c_{H_2O,GDL} - c_{H_2O,AMB}),$$
$$\beta^{H_2O}(c_{H_2O,GDL} - c_{H_2O,AMB}) \ll 1,$$
$$\beta^{O_2}(c_{O_2,GDL} - c_{O_2,AMB}) \ll 1, \quad \beta^{T}(T_{GDL} - T_{AMB}) \ll 1 \tag{20}$$

Here β^T is the thermal volumetric expansion coefficient and β^{O_2} and β^{H_2O} are the solutal volumetric expansion coefficients. The thermal volumetric expansion coefficient is defined as:

$$\beta^{T} = -\frac{1}{\rho}\left(\frac{d\rho}{dT}\right)_p. \tag{21}$$

And the solutal volumetric expansion coefficient is:

$$\beta = \frac{1}{\rho}\left(\frac{d\rho}{dc}\right)_p. \tag{22}$$

Applying this analysis to our standard air breathing fuel cell model simulation provides the results illustrated in Fig. 9. In this figure, the relative contribution from each of the three gradients is plotted as a function of current density for a typical operating condition ($T_{AMB} = 20\,^{\circ}C$, RH = 40%). As shown by the figure, the thermal gradient represents the largest driving force for natural convection, while the water vapor and oxygen gradients show considerably less influence. The oxygen gradient is less important than the water vapor gradient because the molar weight difference between O_2 and N_2 is much smaller than molar weight difference between H_2O and N_2.

5. Conclusions

The one-dimensional, non-isothermal model presented in this paper has been designed to capture the coupling between water generation, oxygen consumption, self-heating and natural convection at the cathode of an air breathing fuel cell. Although simple, the model captures the general trends observed in experimental air breathing fuel cells operated over a wide range of ambient temperatures. The model has been used to explore the major factors determining air breathing fuel cell performance. This analysis has resulted in several important conclusions for the fuel cell parameters explored:

(1) Thermal runaway caused by inadequate heat rejection predominantly limits air breathing fuel cell performance. Oxygen depletion is a less important factor.

(2) In air breathing fuel cells, the natural convection boundary layer represents a significant barrier to mass and heat transfer and is a primary limitation to fuel cell performance. As documented in Table 3, over half of the temperature and concentration drop occurs in the air layer rather than the GDL. Natural convection is therefore a primary limitation in air breathing fuel cell performance.
(3) Because the mass and heat transport numbers associated with natural convection are small, even a minor amount of forced convection (e.g. due to motions of room air) dramatically affects fuel cell behavior.
(4) Optimal air breathing fuel cell design requires maximizing heat rejection while also minimizing the effects of flooding. Decoupling these two phenomena is challenging due to the exponential relationship between water vapor saturation pressure and temperature.

Our model analysis of thermal runaway suggests that air breathing fuel cells should be designed to operate at membrane temperatures below 70 °C in order to avoid catastrophic dry-out. Unfortunately, the model also shows that passive air breathing fuel cell operation at temperatures below 70 °C is complicated by a different water problem: flooding. The contradicting requirements to avoid dry-out but also to avoid flooding reflect the "Goldilocks" problem of air breathing fuel cell operation. In the ideal case, the rates of water generation and removal should match, and not just at one operating point, but across the range of operating conditions and current densities. Aligning the water generation and removal rates over a wide range of operating conditions requires decoupling the water removal rate from its exponential temperature dependence.

Although our model permits tracking of liquid water accumulation, it currently fails to account for deleterious performance losses due to liquid water flooding. As both the model and experimental results indicate, liquid water accumulation is a significant factor in air breathing fuel cell operation at intermediate current densities. A major emphasis of future work will be to implement anode water transport and flooding effects into the fuel cell model.

The conclusions provided by the combined heat and mass transfer air breathing fuel cell cathode model presented in this paper have important design ramifications. One intriguing possibility is to deploy passive heat/mass transport "fin" or "chimney" structures to improve cathode performance by magnifying natural convection. Passive designs to mitigate flooding (via thermal or gravity assist, for example) can also be considered. The fact that even a small degree of forced convection significantly improves performance suggests that even air breathing fuel cells in the 1–5 W power range may benefit from an integrated low-power fan or "gas-stirrer" to improve convection.

Acknowledgement

The authors would like to acknowledge the helpful expertise of Dr. David Barnett on general aspects of the iterative model solution algorithm.

References

[1] C.K. Dyer, J. Power Sources 106 (2002) 31–34.
[2] M. Broussely, G. Archdale, J. Power Sources 136 (2) (2004) 386–394.
[3] T. Hottinen, M. Mikkola, P. Lund, J. Power Sources 129 (2004) 68–72.
[4] C. Ziegler, A. Schmitz, M. Tranitz, E. Fontes, J.O. Schumacher, J. Electrochem. Soc. 151 (12) (2004) A2028–A2041.
[5] T. Hottinen, I. Himanen, P. Lund, J. Power Sources 138 (1–2) (2004) 205–210.
[6] A. Schmitz, M. Tranitz, S. Wagner, et al., J. Power Sources 118 (1–2) (2003) 162–171.
[7] F. Jaouen, S. Haasl, W. van der Wijngaart, et al., J. Power Sources 144 (1) (2005) 113–121.
[8] S. Ha, B. Adams, R.I. Masel, J. Power Sources 128 (2004) 119–124.
[9] J.P. Meyers, H.L. Maynard, J. Power Sources 109 (2002) 76–88.
[10] D. Chu, R. Jiang, J. Power Sources 83 (1999) 128–133.
[11] W. Ying, Y.J. Sohn, W.Y. Lee, J. Ke, C.S. Kim, J. Power Sources 145 (2) (2005) 563–571.
[12] W. Ying, Y.J. Sohn, W.Y. Lee, J. Ke, C.S. Kim, J. Power Sources 145 (2) (2005) 572–581.
[13] P.-W. Li, T. Zhang, Q.-M. Wang, L. Schaefer, M.K. Chyu, J. Power Sources 114 (2003) 63–69.
[14] T. Mennola, M. Noponen, M. Aronniemi, et al., J. Appl. Electrochem. 33 (11) (2003) 979–987.
[15] S. Litster, N. Djilali, Electrochim. Acta 52 (11) (2007) 3849–3862.
[16] S. Litster, J.G. Pharoah, G. McLean, N. Djilali, J. Power Sources 156 (2) (2006) 334–344.
[17] T. Hottinen, M. Noponen, T. Mennola, et al., J. Appl. Electrochem. 33 (3–4) (2003) 265–271.
[18] F.P. Incropera, D.P. DeWitt, Fundamentals of Heat and Mass Transfer, fifth ed., Wiley, NY, 2002.
[19] L.S. Lasdon, A.D. Waren, in: H. Greenberg (Ed.), Design and Implementation of Optimization Software, Sijthoff and Noordhoff Publishers, Alpen aan den Rign, The Netherlands, 1978, pp. 363–397.
[20] R. O'Hayre, S.W. Cha, W. Colella, F.B. Prinz, Fuel Cell Fundamentals, Wiley, NY, 2006.
[21] T. Fabian, J.D. Posner, R. O'Hayre, S.W. Cha, J.K. Eaton, F.B. Prinz, J.G. Santiago, J. Power Sources 161 (2006) 138–142.
[22] T. Fabian, R. O'Hayre, F.B. Prinz, J.G. Santiago, J. Electrochem. Soc, submitted for publication.
[23] Y. Jaluria, Natural Convection and Heat Transfer, Pergamon Press, New York, 1980.
[24] T.E. Springer, T.A. Zawodzinski, S. Gottesfeld, J. Electrochem. Soc. 138 (1991) 2334–2342.
[25] Y. Sone, P. Ekdunge, D. Simonsson, J. Electrochem. Soc. 143 (1996) 1254–1259.
[26] M.L. Perry, J. Newman, E.J. Cairns, J. Electrochem. Soc. 145 (1998) 5–15.
[27] J. Ihonen, M. Mikkola, G. Lindbergh, J. Electrochem. Soc. 151 (8) (2004) A1152.
[28] S. Mitsushima, N. Araki, N. Kamiya, K. Ota, J. Electrochem. Soc. 149 (2002) A1370.
[29] F.A. Uribe, T.E. Springer, S. Gottesfeld, J. Electrochem. Soc. 139 (1992) 765.